

Full Length Article

Laser-assisted preparation of vertically aligned reduced graphene oxide/tannic acid arrays for flexible aqueous zinc-ion hybrid capacitors

Yan Chen ^a, Lijuan Xiao ^a, Yuqi Li ^a, Jianhui Qiu ^b, Limin Zang ^{a,*}, Chao Yang ^a^a Key Laboratory of New Processing Technology for Nonferrous Metal and Materials (Ministry of Education), Guangxi Key Laboratory of Optical and Electronic Materials and Devices, Guangxi Colleges and Universities Key Laboratory of Natural and Biomedical Polymer Materials, Guilin University of Technology, Guilin 541004, China^b Department of Machine Intelligence and Systems Engineering, Faculty of Systems Science and Technology, Akita Prefectural University, Yurihonjo 015-0055, Japan

ARTICLE INFO

ABSTRACT

Keywords:
 Flexible zinc-ion hybrid capacitors
 Carbon materials
 Vertical alignment
 Tannic acid
 Laser assistance

Aqueous zinc-ion hybrid capacitors (AZHCs) are considered an encouraging energy storage candidate owing to their promising environmental benignity and electrochemical performance. To give full play to the advantages of AZHCs, vertically aligned reduced graphene oxide/tannic acid (V-rGO/TA) arrays are constructed on the laser-pre-treated graphite paper (LGP) as flexible carbon-based cathodes (V-rGO/TA/LGP) for AZHCs by a facile laser reduction method. The vertical structure of rGO exhibits abundant physical adsorption sites and ion/electron transfer channels, and the residual oxygen-containing groups of rGO provide favored chemical adsorption sites, which can enhance Zn^{2+} ion storage. In addition, the TA molecules contribute extra capacity by reversible redox reaction (phenol-quinone transition), further improving the electrochemical performance of the electrode. Consequently, the assembled quasi-solid-state AZHC based on the optimized V-rGO/TA/LGP cathode possesses a high specific capacity of $136.6 \mu\text{Ah cm}^{-2}$ and a maximum energy density of $109.3 \mu\text{Wh cm}^{-2}$. In addition, the device exhibits good flexibility with a capacity retention of 97.0 % even after 3000 bending cycles. This design strategy opens up a new approach to construct a vertically aligned carbon material for achieving high-performance flexible AZHCs and realizing their practical applications.

1. Introduction

With the development of flexible electronics with wearable, portable, and foldable characteristics, energy storage devices are required to possess satisfactory electrochemical performance, safety, and flexibility [1–3]. Metal-ion hybrid capacitors are born with the merits of supercapacitors and batteries, showing high energy density, decent power density, and long cycling life [4,5]. Among them, aqueous zinc-ion hybrid capacitors (AZHCs) are of particular interest because Zn metal anode presents the advantages of abundant reserves, low price, low redox potential (-0.76 V vs. standard hydrogen electrode), high theoretical capacity, and good safety, and aqueous electrolytes possess high coulombic efficiency, low cost, and nonflammability [6–9].

Carbon materials have been widely studied as capacitive cathodes for zinc-ion energy storage devices benefiting from their good electrical conductivity, various structures, earth-abundance, and high stability [10–12]. Mass production of graphene oxide (GO) has been achieved at a high-rate and low-cost manufacture via chemical routes, which not only maintains the original two-dimensional structure and high specific

surface area of graphene but also gets fine aqueous electrolyte wettability due to the introduction of oxygen-containing groups [13,14]. Notably, the recent studies on the charge storage mechanism of graphene with abundant oxygen-containing groups in the AZHCs indicate that in addition to the physical adsorption of anions on the surface of graphene, Zn^{2+} ions in the electrolyte can be chemically adsorbed onto the oxygen-containing groups of graphene to contribute extra capacity [15–17]. Nonetheless, the direct use of GO as a cathode material is restricted in practical applications because the serious defects in the carbon net structure of GO are detrimental to its electrical conductivity [18]. Hence, it is essential to obtain reduced GO (rGO) with both proper oxygen-containing groups and abundant ion/electron transfer channels by an effective and facile method in practical terms. Conventional chemical reduction by various reducing agents and thermal reduction at high temperature are still the two mainstream technologies for mass production of rGO, where the commonly used chemical reducing agents (hydrazine, hydroiodic acid, etc.) are highly toxic and many flexible substrates cannot bear harsh conditions [19,20]. Recently, laser reduction of GO has been considered a promising process for obtaining rGO

* Corresponding author.

E-mail address: zanglimin0705@163.com (L. Zang).

because of its technical superiorities for fabrication of graphene-based electronic devices, including patterning, localized treatment, material property tuning, and eco-friendly and convenient processing [18,21,22]. More interestingly, the graphene-based substrates show unique surface morphologies upon laser irradiation [7,23,24]. Compared with the horizontally stacked layer structure, active materials with vertically lamellar structure have large specific surface, and can expose abundant active sites and provide rich ion/electron transfer channels, which endow the cathode with superior electrochemical performance [25,26].

The introduction of redox-active species into carbon-based electrode materials has been proven to be an effective way that can enhance the electrochemical performance owing to the coexistence of carbon electric double-layer capacitive and pseudocapacitive contributions [27–29]. Tannic acid (TA) is a natural polyphenol mixture, which can be extracted from various plant tissues [30,31]. In addition to the advantages of abundance, renewability, non-toxicity and low cost, TA can provide pseudocapacitance by reversible redox reaction (phenol-quinone transition) and have strong interaction with graphene by π - π stacking, indicating it's a promising redox-active modifier for carbon-based electrodes [32–34].

Herein, a layer of GO/TA mixture with different mass ratios was coated on the laser-pretreated graphite paper (LGP), followed by the laser reduction to form the vertically aligned rGO/TA (V-rGO/TA) arrays as flexible cathodes (V-rGO/TA/LGP) for AZHCs in this work. The graphite paper (GP) is regarded as a desired current collector and flexible substrate for flexible energy storage devices owing to its decent electrical conductivity, good flexibility, and light weight [35]. After laser pretreatment, the obtained LGP shows a rough and hydrophilic surface, which can help anchor GO/TA layer. When the GO/TA layer on the surface of LGP is exposed to the semiconductor pulse laser, partial oxygen-containing groups are removed from GO and the original horizontally stacked GO/TA sheets turn to vertically aligned structure, leading to the formation of V-rGO/TA/LGP. Such unique architecture and component design of V-rGO/TA/LGP can provide rich physical/chemical adsorption sites and ion/electron transfer channels for Zn^{2+} ion storage, and the presence of TA molecules can further contribute capacity by reversible redox reaction as well. The effects of mass ratio of GO to TA and laser power on the electrochemical performance of the cathode materials are further investigated. The assembled flexible quasi-solid-state AZHC based on the optimized V-rGO/TA/LGP cathode and Zn foil anode exhibits improved specific capacity, energy density, and bending cycling stability.

2. Experimental section

2.1. Materials

All materials and reagents can be found in [Supporting Information](#).

2.2. Preparation of vertically aligned reduced graphene oxide/tannic acid arrays on the laser-pretreated graphite paper (V-rGO/TA/LGP)

Preparation of LGP: The GP (10 mm × 15 mm) was washed with deionized water. After drying for 6 h at 45 °C, the clean GP was treated by semiconductor pulse laser machine (J3, Dongguan Carving General Intelligent Technology Co., Ltd). Experimental parameters: spot movement speed: 10 mm s⁻¹; wavelength: 450 nm; laser power: 4.5 W; laser scanning are: 10 mm × 10 mm.

Preparation of V-rGO/TA/LGP cathodes: GO dispersion (10.38 g/L) was prepared via a modified Hummers method in advance [36]. Then, four mixtures of GO/TA_n with different mass ratios were prepared by adding a certain amount of TA powder to 4 mL of GO dispersion with constant stirring. Where, n represents the mass ratio of GO/TA ($n = 1:0.1, 1:0.3, 1:0.5$, and $1:1$). The above GO/TA_n mixtures were dropped onto the surface of LGP respectively, and then dried at 45 °C for 6 h. The as-prepared GO/TA_n/LGP samples were treated by the

semiconductor pulse laser (laser wavelength: 450 nm; spot movement speed: 0.4 mm s⁻¹) with various laser powers to obtain the V-rGO/TA_n/LGP_m. Where, m means the laser power ($m = 1.5, 2.25, 3.0, 3.75$, and 4.5 W). At the same time, the V-rGO/LGP_m samples was also prepared in accordance with the above method without the addition of TA (laser wavelength: 450 nm; spot movement speed: 0.4 mm s⁻¹; laser power: 1.5 ~ 4.5 W).

2.3. Assembly of flexible quasi-solid state aqueous zinc-ion hybrid capacitor (AZHC)

A flexible quasi-solid-state AZHC packaged with polyimide film was fabricated by using V-rGO/TA_{1:0.5}/LGP_{3.0} as the cathode, zinc foil as the anode, and membrane soaked in ZnSO₄/gelatin electrolyte as the separator. The preparation process of ZnSO₄/gelatin electrolyte is supplied in the [Supporting Information](#) in detail.

2.4. Characterizations

Scanning electron microscope (FE-SEM, S-4800) was used to observe the morphology of the sample. X-ray diffraction (XRD) patterns were obtained by using a PANalytical X'Pert PRO X-ray diffractometer. Raman spectra were collected by a Thermo Scientific DXR Raman spectroscopy with a laser at 532 nm. X-ray photoelectron spectra (XPS) were obtained by a Thermo Scientific ESCALAB 250Xi with a monochromatic Al K α X-ray source. The surface hydrophilicity of the sample was tested by a contact angle tester (JY-PHB). UV-vis spectra were obtained by an ultraviolet spectrophotometer (UV-9000S), and the pH value of the electrolyte around the cathode was monitored by a pH meter (PHS-25). The electrochemical properties of AZHC based on V-rGO/TA/LGP cathode and zinc foil anode were measured in 2 M ZnSO₄ aqueous solution by CS2350H Bipotentiostat (Wuhan Corrttest Instrument Corp., Ltd). The electrochemical calculations are shown in the [Supporting Information](#).

3. Results and discussion

The design strategy and fabrication process are schematically illustrated in [Fig. 1a](#). The flexible GP with a high electrical conductivity of 10 S cm⁻¹ is selected to serve as flexible substrate and current collector in this work. But it has a relative smooth and hydrophobic surface, which is unfavorable for anchoring active materials. As displayed in [Fig. 1b](#) and [1c](#), the water contact angle decreases from 67° to 0°, demonstrating that the laser pretreatment can increase its hydrophilicity. The digital photographs in [Fig. S1](#) indicate that TA molecules and GO nanosheets can form a stable mixture dispersion owing to the π - π interaction. Then, a uniform layer of GO/TA mixture with different mass ratios was coated onto the surface of LGP. GO has a broad light absorption band, and the localized photothermal effect caused by laser irradiation can remove partial oxygen-containing groups from graphene sheets [18,21]. More than that, laser irradiation also gives rise to the drastic emission of gases such as H₂O and CO₂ during the thermal diffusion process, thereby the V-rGO/TA_n/LGP_m electrodes with a unique vertically aligned structure can be obtained [7,24,37].

The surface morphologies of the electrodes are observed by SEM images as shown in [Fig. 2](#). Compared with the tightly compacted and horizontally stacked laminate structure of GP in [Fig. 2a](#), it is apparent that an array-like structure emerges on the surface of LGP in the laser-scanned region ([Fig. 2b](#)). This rough and hydrophilic surface of LGP is conducive to the anchoring of GO/TA layer. As displayed in [Fig. 2c](#), the sample shows a relatively smooth and uniform surface with some microscopic wrinkles after covering by a layer of GO/TA mixture. Under the laser irradiation of 3.0 W, the horizontally stacked GO/TA sheets turn to vertically aligned arrays while maintaining a relatively complete lamellar structure ([Fig. 2d](#)). The sample of GO/LGP obtained by coating a layer of GO on the surface of LGP also shows a relatively smooth and

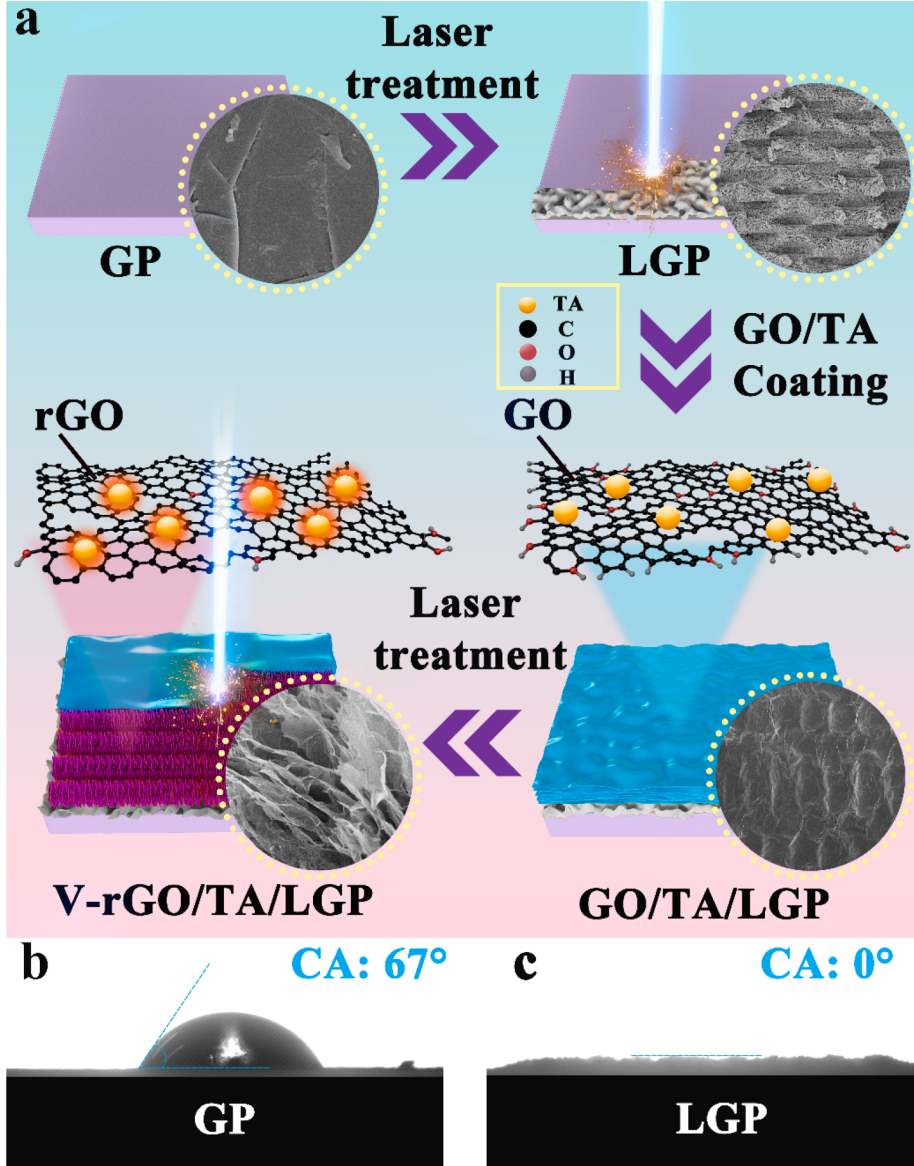


Fig. 1. (a) Schematic fabrication of flexible V-rGO/TA_n/LGP_m electrodes via laser assistance; The water contact angles of (b) original GP and (c) LGP.

uniform surface (Fig. 2e), and the horizontally stacked GO sheets also turn to vertically aligned arrays after undergoing a laser irradiation of 3.0 W. However, the lamellar structure of graphene is severely damaged (Fig. 2f). The significant difference between V-rGO/TA_{1:0.5}/LGP and V-rGO/LGP_{3.0} in morphology demonstrates that the presence of TA molecules can protect the lamellar structure of graphene from damage during the laser reduction process because they can absorb part of the laser energy.

The XRD patterns of the electrode materials are shown in Fig. 3a and b. Two diffraction peaks appearing at 26.7° and 54.6° refer to the (002) and (004) lattice plane of graphite because the GP is applied as the substrate [38]. For the sample of GO/LGP, a new diffraction peak of GO appearing at 11.3° represents the (001) lattice plane [39]. For the sample of GO/TA_{1:0.5}/LGP (Fig. S2), the (001) lattice plane also appears, but the peak strength is weakened and the peak location shifts to the left, indicating that the addition of TA increases the layer spacing between GO sheets [40]. The (001) lattice plane disappears both in the XRD patterns of V-rGO/LGP_{3.0} and V-rGO/TA_{1:0.5}/LGP_{3.0}, which proves that partial oxygen-containing groups have been removed from graphene sheets after the laser reduction process. Raman spectra of GO@LGP, V-rGO/LGP_{3.0} and V-rGO/TA_{1:0.5}/LGP_{3.0} electrodes are

shown in Fig. 3c. Three peaks appear at 1343 cm⁻¹ (D band), 1590 cm⁻¹ (G band), and 2690 cm⁻¹ (2D band), respectively [23,24]. The D band is considered to be the disordered vibration of graphene which indicates the defects in the carbon network structure of graphene, and the G band is the main characteristic peak of graphene due to the planar vibration of sp² graphitic carbon. The value of the I_D/I_G is often used to evaluate the structural defects in carbon-based materials, and a larger value indicates a more defective carbon atomic crystal. The 2D band is mainly the second-order frequency of the D band, reflecting the layer number of multiple graphene sheets. In Fig. 3c, the value of I_D/I_G for GO/LGP and V-rGO/LGP_{3.0} is 0.95 and 0.58 respectively, demonstrating the formation of rGO via laser reduction. The laser beam with a certain energy hits the surface of the GO and instantly generates heat to pyrolyze the oxygen-containing functional groups with weak chemical bonding energy, and some of the sp³ hybridized carbon atoms are reduced to sp² hybridized carbon atoms at the same time [18]. The value of I_D/I_G for V-rGO/TA_{1:0.5}/LGP_{3.0} is 0.80, which is larger than that for V-rGO/LGP_{3.0}. The reason for this result is that the TA molecules absorb part of the energy generated by the laser beam, so the number of oxygen-containing groups on the GO surface that undergo pyrolysis is decreased. That is to say, the relatively low reduction degree of V-rGO/TA_{1:0.5}/LGP_{3.0} is

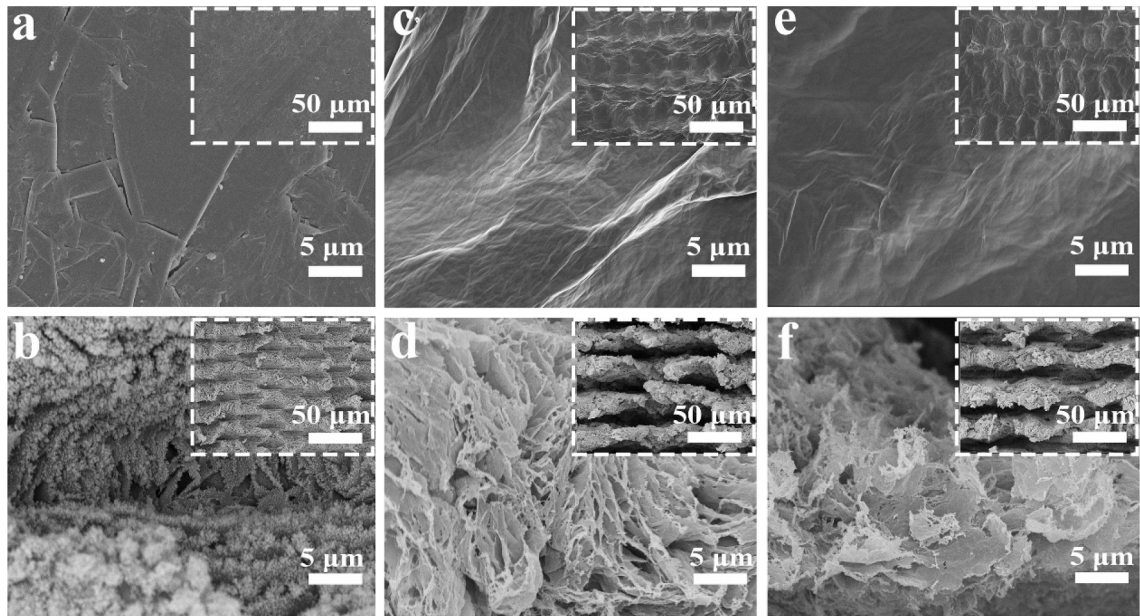


Fig. 2. SEM images of (a) original GP, (b) LGP, (c) GO/TA_{1:0.5}/LGP, (d) V-rGO/TA_{1:0.5}/LGP_{3.0}, (e) GO/LGP, and (f) V-rGO/LGP_{3.0}.

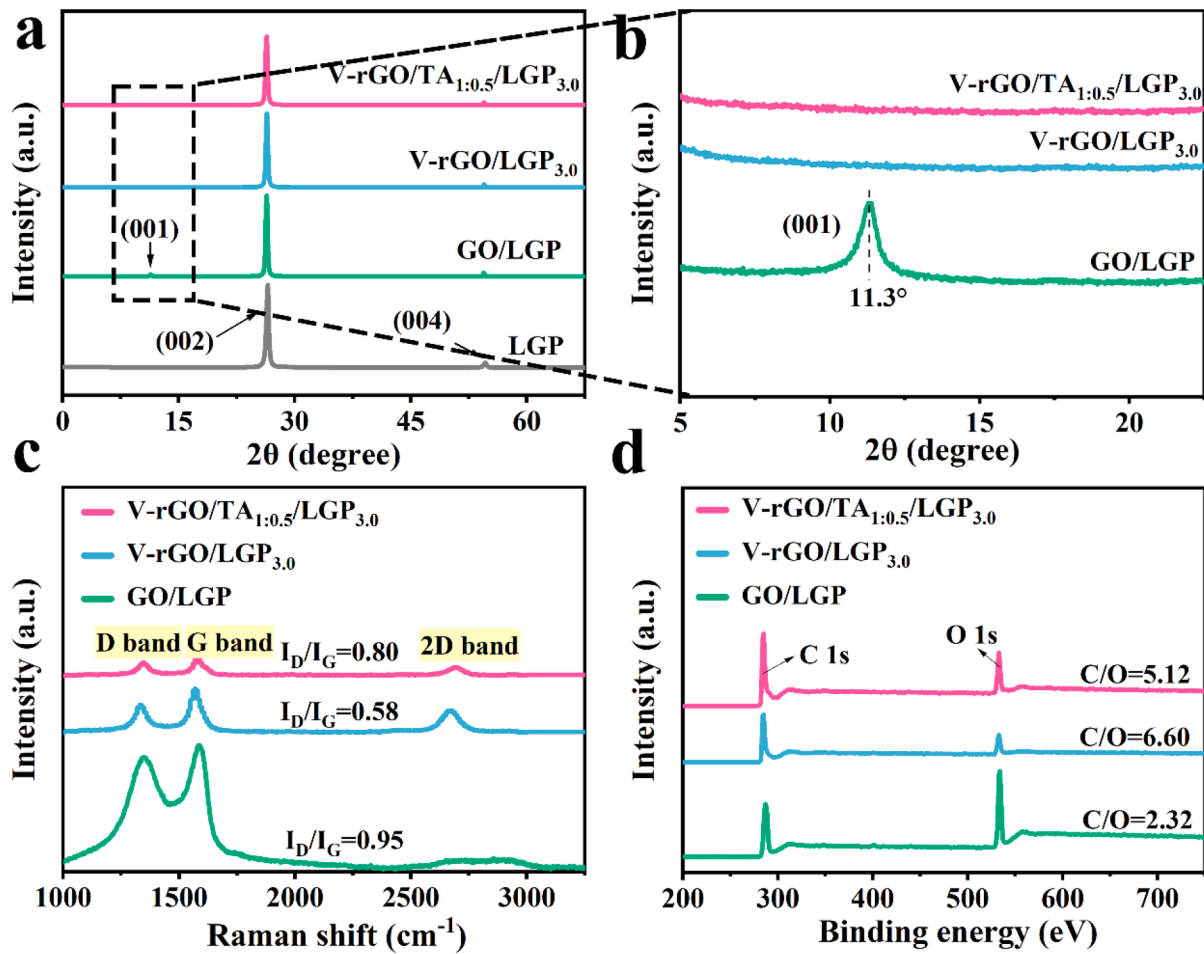


Fig. 3. (a, b) XRD patterns, (c) Raman spectra, and (d) XPS spectra of GO/LGP, V-rGO/LGP_{3.0} and V-rGO/TA_{1:0.5}/LGP_{3.0}.

associated with the introduction of TA molecules. With the increase in the introduction of TA molecules, the reduction degree of GO becomes lower and lower, which is confirmed by the increasing value of I_D/I_G for

V-rGO/TA_n/LGP_{3.0} as shown in Fig. S3a. The reduction degree of GO gets higher and higher with the increasing laser power for both V-rGO/LGP_m (Fig. S3b) and V-rGO/TA_{1:0.5}/LGP_m (Fig. S3c) because more heat

is generated. The influence of laser power on the surface morphology of V-rGO/TA_{1:0.5}/LGP_m is investigated by SEM images. With the laser power increasing from 1.5 to 3.0 W (Fig. S4a-c), the thickness of the vertically aligned arrays becomes thinner and the spacing between the arrays becomes larger, thereby forming rich physical/chemical adsorption sites and ion/electron transfer channels. However, part of the vertically aligned arrays collapse when the laser power increases to 3.75 W (Fig. S4d), and the arrays are seriously damaged when the laser power is 4.5 W (Fig. S4e).

C and O elements are present in the XPS spectra (Fig. 3d), and the atomic concentration ratio of C/O for GO@LGP, V-rGO/LGP_{3.0} and V-rGO/TA_{1:0.5}/LGP_{3.0} is 2.32, 6.60 and 5.12, respectively. The much higher C/O ratios of V-rGO/LGP_{3.0} and V-rGO/TA_{1:0.5}/LGP_{3.0} than that of GO@LGP demonstrate the effective reduction of GO via laser irradiation. In Fig. S5, the C 1 s and O 1 s high-resolution XPS spectra are fitted. The four peaks at 284.6 eV, 286.3 eV, 287.3 eV, and 288.4 eV in C 1 s spectra are attributed to C-C/C = C, C-O, C = O, and O-C = O, respectively [15]. And O 1 s spectra can be deconvoluted into four peaks at 531.6 eV, 532.3 eV, 533.4 eV, and 534.3 eV, which match O-C = O, C = O, C-OH, and C-O-C, respectively [41]. The ratios of carbon-containing and oxygen-containing functional groups are summarized in Table S1 and Table S2, respectively. Significantly, compared with V-rGO/LGP_{3.0}, the relatively high content of oxygen-containing functional groups (especially C-OH) in V-rGO/TA_{1:0.5}/LGP_{3.0} is due to the introduction of TA that contains a large number of phenolic hydroxyl groups. As confirmed by the UV-vis spectra in Fig. S6, TA molecules have bounded on the rGO surface after laser irradiation. Although the presence of TA molecules leads to the relatively low reduction degree of GO, they can protect the lamellar structure of graphene from damage (Fig. 2) and provide extra capacity by reversible redox reaction owing to the phenolic hydroxyl groups in TA, which are beneficial to boost the electrochemical performance.

Fig. S7a schematically illustrates the configuration of the AZHC consisting of V-rGO/TA/LGP as the cathode, zinc foil as the anode, and 2 M ZnSO₄ aqueous solution as the electrolyte. According to the cyclic voltammetry (CV) curves of V-rGO/TA_{1:0.5}/LGP_{3.0}//Zn within different voltage windows (Fig. S7b), 0.2–1.8 V is selected as the voltage window for the subsequent electrochemical tests. The electrochemical properties

of V-rGO/TA_{1:0.5}/LGP_{3.0}//Zn are compared with other AZHCs which use original GP, LGP, and V-rGO/LGP_{3.0} as the cathodes respectively. Nyquist plots of the above four AZHCs are shown in Fig. 4a, and the corresponding values of equivalent series resistance (R_s) and charge transfer resistance (R_{ct}) are summarized in Table S3. The four AZHCs have similar low R_s owing to the high electrical conductivity of GP substrate and good interface between the active materials and GP substrate. GP//Zn has the largest R_{ct} of 522.7 Ω, which is caused by the hydrophobic surface of GP. V-rGO/TA_{1:0.5}/LGP_{3.0}//Zn has the smallest R_{ct} of 120.2 Ω owing to the rich physical/chemical adsorption sites and ion/electron transfer channels of V-rGO/TA_{1:0.5}/LGP_{3.0}.

CV curves at 5 mV s⁻¹ are shown in Fig. 4b and galvanostatic charge-discharge (GCD) curves at 0.2 mA cm⁻² are displayed in Fig. 4c. As expected, V-rGO/TA_{1:0.5}/LGP_{3.0}//Zn exhibits the largest enclosed CV area and longest discharge time, indicating it has the highest specific capacity. The specific capacity of GP//Zn, LGP//Zn, V-rGO/LGP_{3.0}//Zn, and V-rGO/TA_{1:0.5}/LGP_{3.0}//Zn at 0.2 mA cm⁻² is 14.2, 32.7, 51.0, and 141.0 μAh cm⁻², respectively. Among them, GP//Zn possesses the smallest specific capacity due to the smooth and hydrophobic surface as well as the limited charge storage mechanism of GP through physical adsorption/desorption. After laser pretreatment, the rough and hydrophilic surface of LGP is conducive to the physical adsorption of electrolyte ions, which can enhance the specific capacity. For V-rGO/LGP_{3.0}//Zn, besides physical adsorption/desorption, Zn²⁺ ions are also chemically adsorbed onto the residual oxygen-containing groups of rGO to contribute extra capacity. The charge storage mechanism of V-rGO/TA_{1:0.5}/LGP_{3.0} cathode is complex due to its unique architecture and component design. Theoretically, the large specific surface can provide rich physical adsorption sites, proper oxygen-containing groups of rGO can offer abundant chemical adsorption sites, vertically aligned arrays can supply many ion transfer channels, proper reduction degree of rGO can endow electron transfer channels, and redox electroactive molecules (TA) can contribute pseudocapacitance, thus V-rGO/TA_{1:0.5}/LGP_{3.0}//Zn exhibits the highest specific capacity.

In order to further reveal the charge storage mechanism of V-rGO/TA/LGP cathodes in AZHC, the V-rGO/TA_{1:0.5}/LGP_{3.0} cathode during charge-discharge process was comprehensively investigated through *in-situ* and *ex-situ* tests. Fig. 4d records the pH values of the electrolyte

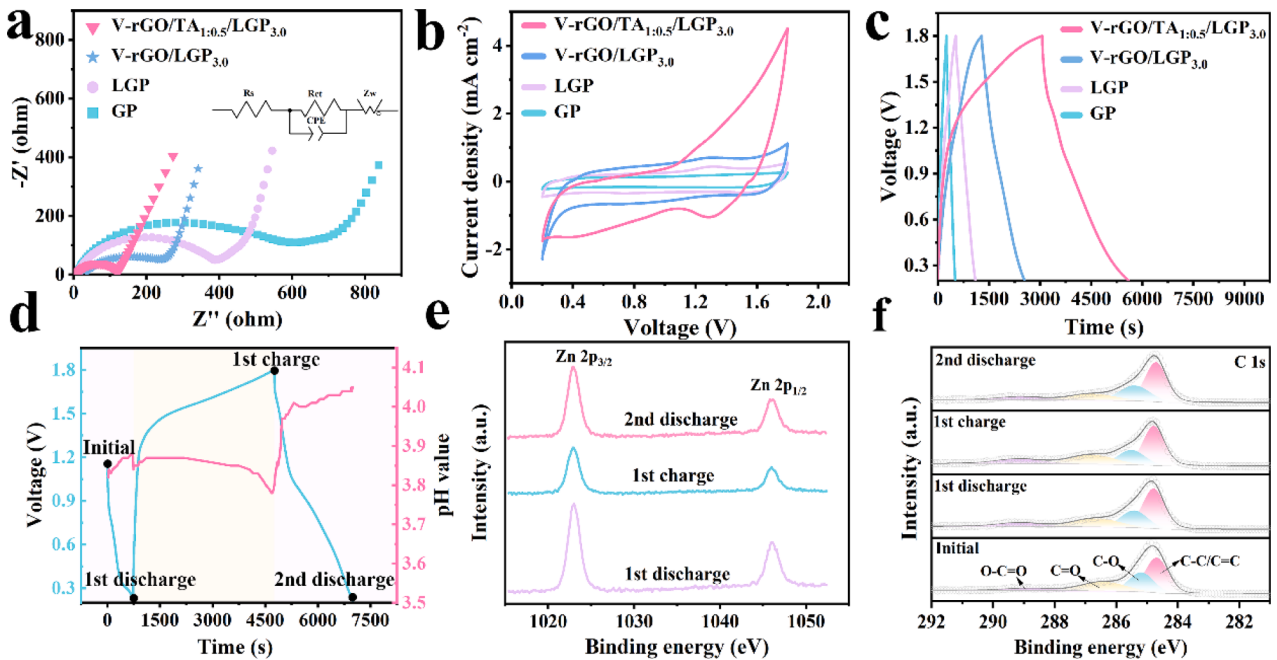
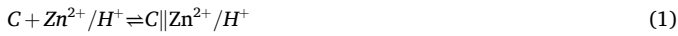


Fig. 4. (a) Nyquist plots, (b) CV curves at 5 mV s⁻¹, and (c) GCD curves at 0.2 mA cm⁻² of various AZHCs in 2 M ZnSO₄; (d) pH values of the electrolyte around the V-rGO/TA_{1:0.5}/LGP_{3.0} cathode, and (e) Zn 2p and (f) C 1s high-resolution XPS spectra of the V-rGO/TA_{1:0.5}/LGP_{3.0} cathode during charge-discharge process.

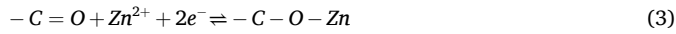
around the V-rGO/TA_{1:0.5}/LGP_{3.0} cathode during the charge–discharge process. During the first discharge process (initial state to 0.2 V), the pH value shows an upward trend, indicating that H⁺ is moved to the surface/inner of the cathode, resulting in an increase in the concentration of OH⁻ in the electrolyte around the cathode. However, the pH value shows a downward trend during the subsequent charge process (0.2 V to 1.8 V), demonstrating that H⁺ is released from the cathode and returns to the solution, resulting in an increase in the concentration of H⁺ in the electrolyte around the cathode. During the second discharge process (1.8 V to 0.2 V), the pH value shows an upward trend, proving that H⁺ is moved to the cathode again. The pH change of the electrolyte around the cathode is visually observed in Fig. S8a, which further reveals the reversible movement of H⁺ to the cathode during charge–discharge process. *Ex-situ* Zn 2p and C 1 s high-resolution XPS spectra of the V-go/TA_{1:0.5}/LGP_{3.0} cathode at different voltages during charge–discharge process were conducted to analyze its surface chemical states. The Zn 2p signal first enhances at the first fully discharged state, then weakens at the first fully charged state, and enhances again at the second fully discharged state (Fig. 4e), indicating that Zn²⁺ can be reversibly moved to the surface/inner of the cathode. Fig. 4f and Fig. S8b record the corresponding changes in the contents of four carbon-containing functional groups at four voltage states. In particular, the content of C = O decreases at the first fully discharged state, then increases at the first fully charged state, and decreases again at the second fully discharged state. Meanwhile, the change of the content of C-O has the opposite trend. The possible charge storage process of V-rGO/TA/LGP//Zn is summarized in Equations (1)–(6) [32,42,43]. Fig. S9 shows the rate performance of the four AZHCs from 0.2 to 1.0 mA cm⁻², and V-rGO/TA_{1:0.5}/LGP_{3.0}//Zn possesses relatively poor rate performance due to its complex charge storage process. When the current density is high, it doesn't have enough time to complete the chemical adsorption/desorption and redox reactions, resulting in the low specific capacity. Even so, V-rGO/TA_{1:0.5}/LGP_{3.0}//Zn still exhibits higher specific capacity than other AZHCs in the whole testing range owing to its multiple charge storage reactions.

Charge storage of cathode:

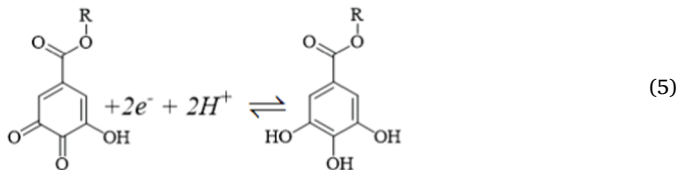
1) Physical adsorption/desorption



2) Chemical adsorption/desorption



3) Redox reaction



Charge storage of anode:
Electroplating/stripping



To investigate the effect of laser power on the electrochemical properties, the LGP pretreated with different laser power is used as the cathode and zinc foil is used as the anode to perform the electrochemical tests in 2 M ZnSO₄. According to the results shown in Fig. S10 and the detailed analyses discussed in the Supporting Information, LGP

pretreated with 4.5 W has the highest specific capacity and the best rate performance, which is selected for the following work. Fig. 5a-c explores the influence of the mass ratio of GO/TA on the electrochemical properties of V-rGO/TA_n/LGP_{3.0}//Zn AZHCs in 2 M ZnSO₄. As shown in Fig. 5a and 5b, with the successive increase in TA content from 1:0.1 to 1:0.5, the enclosed CV area gradually becomes larger, and the discharge time in the GCD curve also keeps lengthening. When the TA content further increases and the mass ratio of GO/TA is 1:1, the enclosed CV area gets smaller, and the discharge time in the GCD curve is shortened. The specific capacity of V-rGO/TA_{1:0.1}/LGP_{3.0}//Zn, V-rGO/TA_{1:0.3}/LGP_{3.0}//Zn, V-rGO/TA_{1:0.5}/LGP_{3.0}//Zn, and V-rGO/TA_{1:1}/LGP_{3.0}//Zn at 0.2 mA cm⁻² is 85.6, 105.8, 141.0, and 107.1 μAh cm⁻², respectively. The introduction of TA can play multiple roles in this work. As discussed above, the presence of TA can provide extra pseudo-capacity via reversible redox reaction and protect the lamellar structure of graphene from damage, which is conducive to the improvement of the electrochemical performance. On the other hand, the introduction of TA can cause relatively low reduction degree of GO. More importantly, as schematically illustrated in the left diagram in Fig. 5g, many vertically aligned rGO sheets are bonded when the mass ratio of GO/TA is 1:1. This phenomenon can reduce the physical/chemical adsorption sites and ion/electron transfer channels, thus leading to the larger R_{ct} and lower specific capacity than those of V-rGO/TA_{1:0.5}/LGP_{3.0}//Zn. As confirmed by the Nyquist plots in Fig. 5c and the corresponding R_{ct} values in Table S4, the R_{ct} of V-rGO/TA_{1:1}/LGP_{3.0}//Zn is 247.3 Ω, which is much higher than that of V-rGO/TA_{1:0.5}/LGP_{3.0}//Zn (120.2 Ω).

The effect of laser reduction power on the electrochemical properties of V-rGO/TA_{1:0.5}/LGP_m//Zn AZHCs in 2 M ZnSO₄ is also taken into account. As continuous pulses sweep across the surface, the locally accumulated temperature ablates the surface, and gases such as H₂O, CO₂, and CO spill out, generating a rich porous laminar structure and increasing the effective area for ion diffusion [18]. As displayed in Fig. 5d, the enclosed CV area first increases and then decreases with the increase in laser reduction power. Consistent with CV results, the discharge time in the GCD curve also first increases and then decreases as the laser reduction power increases (Fig. 5e). The specific capacity of V-rGO/TA_{1:0.5}/LGP_{1.5}//Zn, V-rGO/TA_{1:0.5}/LGP_{2.25}//Zn, V-rGO/TA_{1:0.5}/LGP_{3.0}//Zn, V-rGO/TA_{1:0.5}/LGP_{3.75}//Zn, and V-rGO/TA_{1:0.5}/LGP_{4.5}//Zn at 0.2 mA cm⁻² is 88.8, 96.0, 141.0, 119.6, and 109.6 μAh cm⁻², respectively. From the perspective of the specific capacity, the optimum laser reduction power is confirmed to be 3.0 W. Excessive laser reduction power can destroy the vertically aligned array architecture (Fig. S4), resulting in the physical/chemical adsorption sites and ion/electron transfer channels being damaged as schematically illustrated in the middle diagram in Fig. 5g. Although increasing the laser reduction power is beneficial to improve the reduction degree of GO, the broken vertically aligned array structure can cause a large R_{ct} and a low specific capacity. Based on the Nyquist plots in Fig. 5f and the corresponding R_{ct} values in Table S5, the R_{ct} of V-rGO/TA_{1:0.5}/LGP_{4.5}//Zn is as high as 207.1 Ω, which is much higher than that of V-rGO/TA_{1:0.5}/LGP_{3.0}//Zn (120.2 Ω). According to the specific capacities at various current densities from 0.2 to 1.0 mA cm⁻², V-rGO/TA_{1:0.5}/LGP_{3.0}//Zn has the highest specific capacity among all V-rGO/TA_n/LGP_{3.0}//Zn and V-rGO/TA_{1:0.5}/LGP_m//Zn AZHCs in the whole testing range (Fig. S11) due to the rich physical/chemical adsorption sites and ion/electron transfer channels as schematically illustrated in the right diagram in Fig. 5g.

Owing to the unique architecture and component design of V-rGO/TA_{1:0.5}/LGP_{3.0}, V-rGO/TA_{1:0.5}/LGP_{3.0}//Zn possesses multiple charge storage mechanisms and exhibits good electrochemical performance. Fig. 5h shows the CV curves of a V-rGO/TA_{1:0.5}/LGP_{3.0}//Zn in 2 M ZnSO₄ at low scan rates of 1–10 mV s⁻¹, which are used to analyze the capacitive-controlled charge contribution (k_1v) and the diffusion-controlled charge contribution ($k_2v^{1/2}$) to the total charge storage based on Equation (7) [44]:

$$i = k_1v + k_2v^{1/2} \quad (7)$$

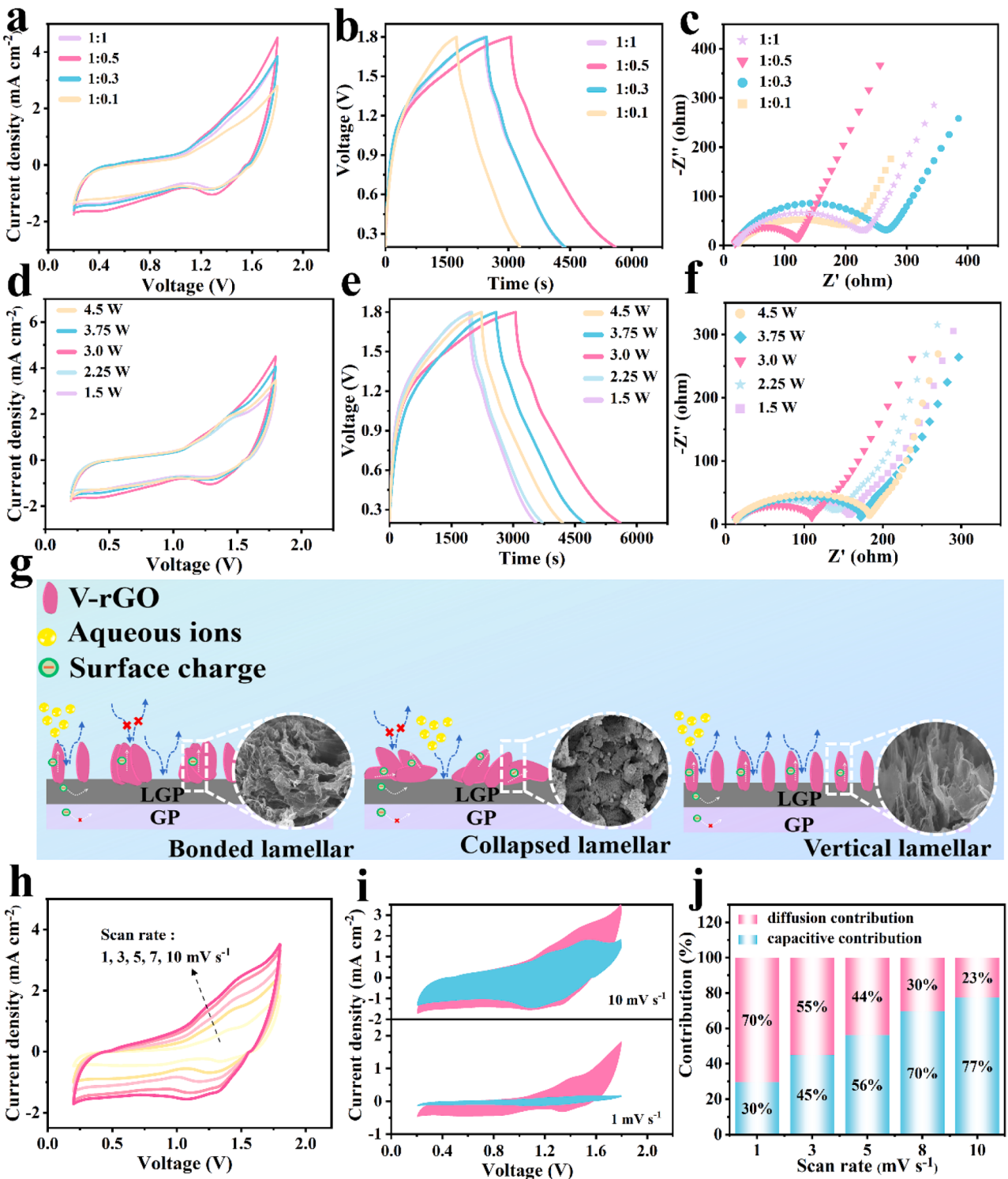


Fig. 5. (a) CV curves at 5 mV s⁻¹, (b) GCD curves at 0.2 mA cm⁻², and (c) Nyquist plots of V-rGO/TA_n/LGP_{3.0}//Zn AZHCs in 2 M ZnSO₄. (d) CV curves at 5 mV s⁻¹, (e) GCD curves at 0.2 mA cm⁻², and (f) Nyquist plots of V-rGO/TA_{1:0.5}/LGP_{3.0}//Zn AZHCs in 2 M ZnSO₄. (g) Schematic illustration of physical/chemical adsorption sites and ion/electron transfer channels of various AZHCs in 2 M ZnSO₄. Electrochemical kinetic analysis of V-rGO/TA_{1:0.5}/LGP_{3.0}//Zn AZHC in 2 M ZnSO₄: (h) CV curves at 1–10 mV s⁻¹; (i) Capacitive-controlled contributions at 1 mV s⁻¹ and 10 mV s⁻¹; (j) Percentages of capacitive-controlled contribution at 1–10 mV s⁻¹.

where i represents the current, v is the scan rate, and k_1 and k_2 are constants. The blue and pink regions in Fig. 5i represent the capacitive-controlled contribution and diffusion-controlled contribution at 1 mV s⁻¹ and 10 mV s⁻¹, respectively. As shown in Fig. 5j, the percentages of capacitive-controlled contribution at 1, 3, 5, 8, and 10 mV s⁻¹ are 30 %, 45 %, 56 %, 70 %, and 77 %, respectively. The

diffusion-controlled process is the dominant contribution at relatively low scan rates, while the capacitive-controlled process plays an important role at relatively high scan rates due to the limitation of ion diffusion.

To verify the practicability in wearable and foldable electronics, the V-rGO/TA_{1:0.5}/LGP_{3.0} cathode and zinc foil anode are assembled into a sandwich-like flexible quasi-solid-state AZHC using membrane soaked

in ZnSO_4 /gelatin electrolyte as the separator and polyimide film as the packing material. Fig. 6a exhibits almost similar CV curves at 5–100 mV s⁻¹ with no polarization, demonstrating its good electrochemical kinetics. Based on the GCD curves shown in Fig. 6b, the specific capacity of the quasi-solid-state AZHC at 0.2 mA m⁻² is 136.6 $\mu\text{Ah cm}^{-2}$, which is only a little lower than that of V-rGO/TA_{1:0.5}/LGP_{3.0}//Zn in 2 M ZnSO_4 (141.0 $\mu\text{Ah cm}^{-2}$). The high specific capacity of the device is attributed to the rich physical/chemical adsorption sites and ion/electron transfer channels of V-rGO/TA_{1:0.5}/LGP_{3.0}. By the same token, the R_s and R_{ct} values of the device fitted by the Nyquist plot (Fig. 6c) are 9.2 Ω and 152.1 Ω , respectively, which are a little higher than those of V-rGO/TA_{1:0.5}/LGP_{3.0}//Zn in 2 M ZnSO_4 . The cycling stability of the device is evaluated and the result is shown in Fig. 6d. The device achieves a capacity retention of 70.0 % after 5000 GCD cycles at 4 mA cm⁻², and a Coulombic efficiency of 99.8 % during this GCD cycling. Ragone plots of this device are given in Fig. 6e and compared with other zinc-ion energy storage devices [36,45–50]. In this work, the quasi-solid-state V-rGO/TA_{1:0.5}/LGP_{3.0}//Zn provides the highest energy density of 109.3 $\mu\text{Wh cm}^{-2}$ (power density of 160.0 $\mu\text{W cm}^{-2}$) and power density of 800.0 $\mu\text{W cm}^{-2}$ (energy density of 34.4 $\mu\text{Wh cm}^{-2}$), respectively. As shown in Fig. 6f, three devices connected in series can light up an LED with an operating voltage of 3 V. The electrochemical performance under various bending conditions serves as an important evaluation tool to assess flexible energy storage devices. In Fig. 6g and Fig. S12, the

device is bent into different angles from 0 to 150°, and all CV curves almost overlap. In addition, after 3000 bending cycles (0° to 150° to 0°), the capacity retention of the device is still as high as 97.0 % (Fig. 6h), which further indicates that the device has excellent flexibility and electrochemical stability. Table S6 summarizes the electrochemical performance of the quasi-solid-state V-rGO/TA_{1:0.5}/LGP_{3.0}//Zn and other recently reported zinc-ion energy storage devices, which demonstrates the superiority and promising application prospect of V-rGO/TA/LGP as cathodes for AZHCs.

4. Conclusion

Overall, the simple, fast, and green laser technique is applied to prepare high-performance flexible cathodes for AZHCs by using GP as the flexible substrate/current collector and GO/TA as the raw active material. The GP after laser irradiation has a rough and hydrophilic surface, and partial oxygen-containing groups are removed from GO to form rGO via laser irradiation. The reduction degree of GO, morphology, and electrochemical properties of the cathode materials are affected by both the mass ratio of GO to TA and laser power. From the perspective of the electrochemical performance, the optimized mass ratio of GO/TA is confirmed to be 1:0.5, and the optimized laser for pretreatment of GP and reduction of GO are 4.5 W and 3.0 W, respectively. The cathode material prepared under optimum conditions (V-rGO/TA_{1:0.5}/LGP_{3.0})

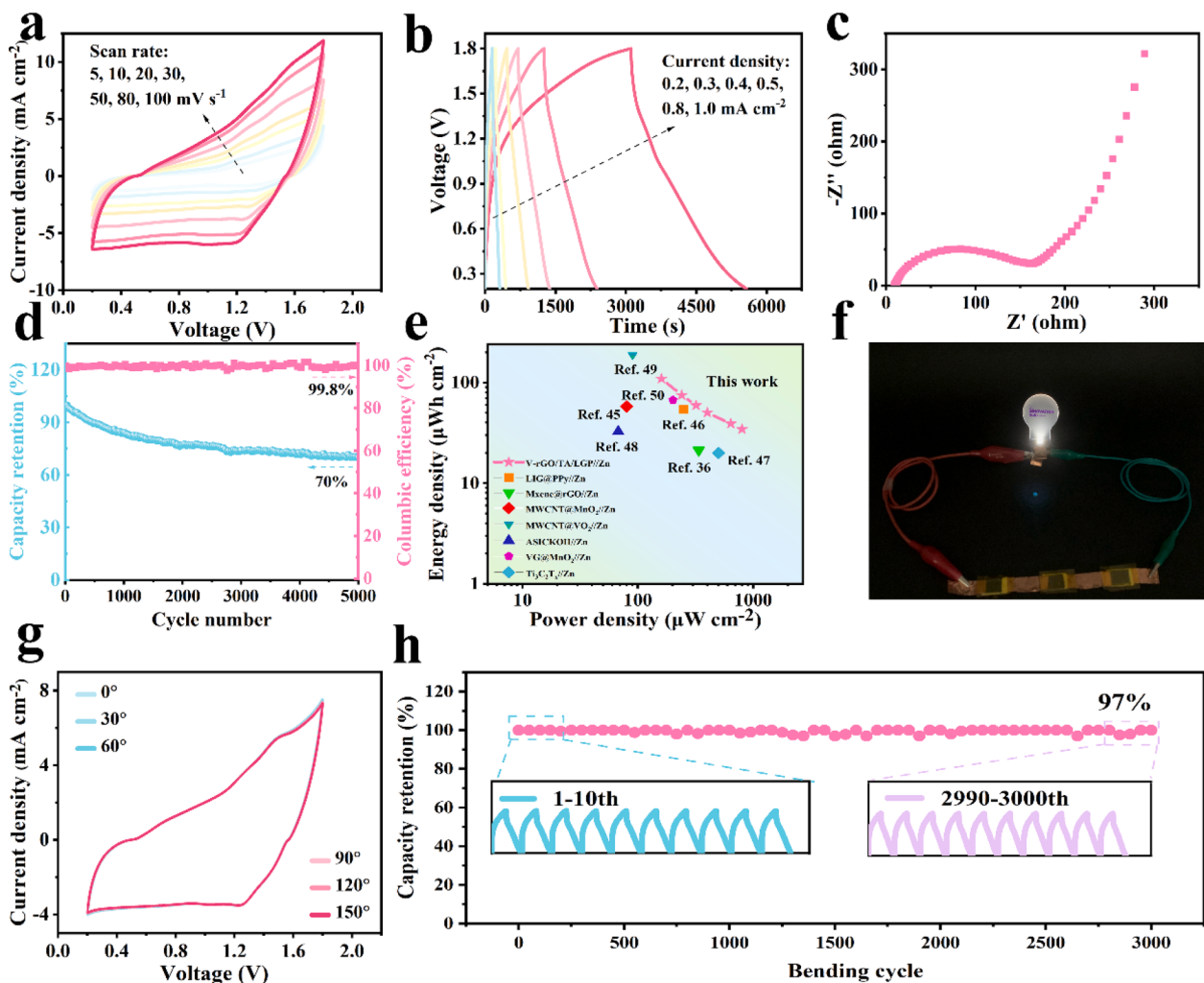


Fig. 6. Electrochemical properties of the quasi-solid-state AZHC: (a) CV curves; (b) GCD curves; (c) Nyquist plot; (d) Cycling stability and Coulombic efficiency at 4 mA cm⁻²; (e) Ragone plots; (f) Digital photo of a LED lightened by three devices connected in series; (g) CV curves at various bending angles; (h) Bending cycling stability at 4 mA cm⁻².

has vertically aligned arrays which consist of rGO with proper oxygen-containing groups and TA with redox activity. This unique architecture and component design can provide abundant physical/chemical adsorption sites and ion/electron transfer channels, which is beneficial to play its multiple charge storage mechanisms and show good electrochemical performance. The quasi-solid-state V-rGO/TA_{1.0.5}/LGP_{3.0//Zn} device achieves a maximum specific capacity of 136.6 μAh cm⁻², energy density of 109.3 μWh cm⁻², and power density of 800.0 μW cm⁻². At the same time, suffering from 5000 GCD cycles, the specific capacity of the device remains 70.0 % of its initial value. Also, the capacity retention of the device can be maintained at 97.0 % after 3000 bending cycles owing to the flexible GP substrate. In conclusion, this work provides a feasible and simple method to obtain high-performance cathode materials with vertically aligned arrays by laser assistance, which plays a positive role in promoting the application of AZHCs in flexible electronics.

CRediT authorship contribution statement

Yan Chen: Writing – original draft, Software, Investigation, Data curation. **Lijuan Xiao:** Validation, Investigation, Data curation. **Yuqi Li:** Validation, Software. **Jianhui Qiu:** Methodology. **Limin Zang:** Writing – review & editing, Supervision, Funding acquisition, Conceptualization. **Chao Yang:** Writing – review & editing, Methodology, Funding acquisition.

Declaration of competing interest

The authors declare that they have no known competing financial interests or personal relationships that could have appeared to influence the work reported in this paper.

Data availability

Data will be made available on request.

Acknowledgments

This work was supported by the National Natural Science Foundation of China (52263016); the Natural Science Foundation of Guangxi Province (2023GXNSFAA026162); the Natural Science Foundation of Guangxi Province (AB23075171); the National Natural Science Foundation of China (22265007); and the Science and Technology Plan of Guilin (ZY20220101).

Appendix A. Supplementary material

Supplementary data to this article can be found online at <https://doi.org/10.1016/j.apsusc.2024.160230>.

References

- [1] W. Li, J. Liu, J. Wei, Z. Yang, C. Ren, B. Li, Recent progress of conductive hydrogel fibers for flexible electronics: Fabrications, applications, and perspectives, *Adv. Funct. Mater.* 33 (2023) 2213485, <https://doi.org/10.1002/adfm.202213485>.
- [2] S. Gong, Y. Shi, Y. Su, F. Qi, Y. Song, G. Yang, B. Li, X. Wu, J. Zhang, C. Tong, H. Sun, Introduction of S-S bond to flexible supercapacitors for high mass specific capacity and stability, *J. Alloy. Compd.* 911 (2022) 165080, <https://doi.org/10.1016/j.jallcom.2022.165080>.
- [3] S. Gong, Y. Li, Y. Su, B. Li, G. Yang, X. Wu, J. Zhang, H. Sun, Y. Li, Construction of bimetallic heterojunction based on porous engineering for high performance flexible asymmetric supercapacitors, *Small* 19 (2023) 2205936, <https://doi.org/10.1002/smll.202205936>.
- [4] M. Wu, W. Zheng, X. Hu, F. Zhan, Q. He, H. Wang, Q. Zhang, L. Chen, Exploring 2D energy storage materials: Advances in structure, synthesis, optimization strategies, and applications for monovalent and multivalent metal-ion hybrid capacitors, *Small* 18 (2022) 2205101, <https://doi.org/10.1002/smll.202205101>.
- [5] N.T. Aristote, X. Deng, K. Zou, X. Gao, R. Momen, F. Li, W. Deng, H. Hou, G. Zou, X. Ji, General overview of sodium, potassium, and zinc-ion capacitors, *J. Alloy. Compd.* 913 (2022) 165216, <https://doi.org/10.1016/j.jallcom.2022.165216>.
- [6] D. Li, Y. Tang, S. Liang, B. Lu, G. Chen, J. Zhou, Self-assembled multilayers direct a buffer interphase for long-life aqueous zinc-ion batteries, *Energy Environ. Sci.* 16 (2023) 3381–3390, <https://doi.org/10.1039/D3EE01098H>.
- [7] X. Zhong, C. Yang, Y. Zhao, J. Qiu, L. Zang, Rational design of layered MnO₂@graphene with hierarchical structure for flexible quasisolid-state aqueous zinc-ion battery via laser activation, *Adv. Mater. Technol.* 8 (2023) 2201430, <https://doi.org/10.1002/admt.202201430>.
- [8] C. Wang, X. Zeng, P.J. Cullen, Z. Pei, The rise of flexible zinc-ion hybrid capacitors: advances, challenges, and outlooks, *J. Mater. Chem. A* 9 (2021) 19054–19082, <https://doi.org/10.1039/DITA02775A>.
- [9] M. Wen, C. Yang, Q. Liu, J. Qiu, L. Zang, Wide-potential-window bimetallic hydrated eutectic electrolytes with high-temperature resistance for zinc-ion hybrid capacitors, *Small* 19 (2023) 2303348, <https://doi.org/10.1002/smll.202303348>.
- [10] X. Gao, H. Wu, C. Su, C. Lu, Y. Dai, S. Zhao, X. Hu, F. Zhao, W. Zhang, I.P. Parkin, C.J. Carmalt, G. He, Recent advances in carbon-based nanomaterials for multivalent-ion hybrid capacitors: A review, *Energy Environ. Sci.* 16 (2023) 1364–1383, <https://doi.org/10.1039/D2EE03719J>.
- [11] Z. Dang, X. Li, Y. Li, L. Dong, Heteroatom-rich carbon cathodes toward high-performance flexible zinc-ion hybrid supercapacitors, *J. Colloid Interface Sci.* 644 (2023) 221–229, <https://doi.org/10.1016/j.jcis.2023.04.074>.
- [12] Z. Wang, M. Zhang, W. Ma, J. Zhu, W. Song, Application of carbon materials in aqueous zinc ion energy storage devices, *Small* 17 (2021) 2100219, <https://doi.org/10.1002/smll.202100219>.
- [13] Y. Tian, Z. Yu, L. Cao, X.L. Zhang, C. Sun, D.W. Wang, Graphene oxide: An emerging electromaterial for energy storage and conversion, *J. Energy Chem.* 55 (2021) 323–344, <https://doi.org/10.1016/j.jechem.2020.07.006>.
- [14] M. Gautam, S. Kanade, B.B. Kale, Electrochemical energy storage and conversion applications of graphene oxide: A review, *Energy Fuels* 37 (2023) 17134–17160, <https://doi.org/10.1021/acs.energyfuels.3c02933>.
- [15] Y. Shao, Z. Sun, Z. Tian, S. Li, G. Wu, M. Wang, X. Tong, F. Shen, Z. Xia, V. Tung, J. Sun, Y. Shao, Regulating oxygen substituents with optimized redox activity in chemically reduced graphene oxide for aqueous Zn-ion hybrid capacitor, *Adv. Funct. Mater.* 31 (2021) 2007843, <https://doi.org/10.1002/adfm.202007843>.
- [16] G. Sun, Y. Xiao, B. Lu, X. Jin, H. Yang, C. Dai, X. Zhang, Y. Zhao, L. Qu, Hybrid energy storage device: Combination of zinc-ion supercapacitor and zinc-air battery in mild electrolyte, *ACS Appl. Mater. Interfaces* 12 (2020) 7239–7248, <https://doi.org/10.1021/acsami.9b20629>.
- [17] M. Wen, X. Yu, C. Yang, J. Qiu, L. Zang, Compressible zinc-ion hybrid supercapacitor and piezoresistive sensor based on reduced graphene oxide/polypyrrole modified melamine sponge, *Polym. Compos.* 44 (2023) 3843–3855, <https://doi.org/10.1002/pc.27360>.
- [18] R. You, Y.Q. Liu, Y.L. Hao, D.D. Han, Y.L. Zhang, Z. You, Laser fabrication of graphene-based flexible electronics, *Adv. Mater.* 32 (2020) 1901981, <https://doi.org/10.1002/adma.201901981>.
- [19] S. Verma, T. Das, V.K. Pandey, B. Verma, Facile and scalable synthesis of reduced-graphene oxide using different green reducing agents and its characterizations, *Diam. Relat. Mat.* 129 (2022) 109361, <https://doi.org/10.1016/j.diamond.2022.109361>.
- [20] P. Zhang, Z. Li, S. Zhang, G. Shao, Recent advances in effective reduction of graphene oxide for highly improved performance toward electrochemical energy storage, *Energy Environ. Mater.* 1 (2018) 5–12, <https://doi.org/10.1002/eem.212001>.
- [21] R. Kumar, A.P. del Pino, S. Sahoo, R.K. Singh, W.K. Tan, K.K. Kar, A. Matsuda, E. Joanni, Laser processing of graphene and related materials for energy storage: State of the art and future prospects, *Prog. Energy Combust. Sci.* 91 (2022) 100981, <https://doi.org/10.1016/j.pecs.2021.100981>.
- [22] T.X. Tran, H. Choi, C.H. Che, J.H. Sul, I.G. Kim, S.M. Lee, J.H. Kim, J.B. In, Laser-induced reduction of graphene oxide by intensity-modulated line beam for supercapacitor applications, *ACS Appl. Mater. Interfaces* 10 (2018) 39777–39784, <https://doi.org/10.1021/acsami.8b14678>.
- [23] Q. Li, Y. Ding, L. Yang, L. Li, Y. Wang, Periodic nanopatterning and reduction of graphene oxide by femtosecond laser to construct high-performance micro-supercapacitors, *Carbon* 172 (2021) 144–153, <https://doi.org/10.1016/j.carbon.2020.09.096>.
- [24] S. Park, S. Ji, Y. Yoon, S.K. Kim, W. Song, S. Myung, J. Lim, H.K. Jung, S.S. Lee, K. S. An, Fabrication of fanlike L-shaped graphene nanostructures with enhanced thermal/electrochemical properties via laser irradiation, *Carbon* 182 (2021) 691–699, <https://doi.org/10.1016/j.carbon.2021.05.045>.
- [25] X. Li, Y. Li, X. Zhao, F. Kang, L. Dong, Elucidating the charge storage mechanism of high-performance vertical graphene cathodes for zinc-ion hybrid supercapacitors, *Energy Storage Mater.* 53 (2022) 505–513, <https://doi.org/10.1016/j.ensm.2022.09.023>.
- [26] S. Gong, Y. Shi, Y. Su, Y. Li, L. Ding, J. Lin, G. Yang, B. Li, X. Wu, J. Zhang, H. Xie, H. Sun, In situ growth of 3D lamellar Mn(OH)₂ on CuO-coated carbon cloth for flexible asymmetric supercapacitors with a high working voltage of 2.4 V, *ACS Sustainable Chem. Eng.* 9 (2021) 13385–13394, <https://doi.org/10.1021/acssuschemeng.1c05164>.
- [27] C. Liang, L. Zang, F. Shi, C. Yang, J. Qiu, Q. Liu, Z. Chen, High-performance cotton fabric-based supercapacitors consisting of polypyrrole/Ag/graphene oxide nanocomposite prepared via UV-induced polymerization, *Cellulose* 29 (2022) 2525–2537, <https://doi.org/10.1007/s10570-022-04454-4>.
- [28] A. Paul, P. Samanta, H. Kolya, C.W. Kang, N.C. Murmu, T. Kuila, Rational design of asymmetric aqueous supercapacitor based on the composites of reduced graphene oxide with manganese-doped nickel sulfide-tin sulfide as positive electrode and manganese sulfide negative electrode, *J. Power Sources* 580 (2023) 23352, <https://doi.org/10.1016/j.jpowsour.2023.23352>.

- [29] H. Wang, W. Jiang, S. Chen, J. Chen, F. Wu, R. Liang, Epitaxial oriented growth of LDH on few-layer graphene/microporous carbon heterostructure sheets for asymmetric supercapacitor application, *Chem. Eng. J.* 474 (2023) 145755, <https://doi.org/10.1016/j.cej.2023.145755>.
- [30] S. Zhou, Q. Wei, H. Fan, Y. Zhang, G. Gao, X. Hu, Cross-linking and self-assembly synthesis of tannin-based carbon frameworks cathode for Zn-ion hybrid supercapacitors, *J. Colloid Interf. Sci.* 644 (2023) 478–486, <https://doi.org/10.1016/j.jcis.2023.04.112>.
- [31] Z. Zheng, D. Ren, Y. Li, F. Kang, X. Li, X. Peng, L. Dong, Self-assembled robust interfacial layer for dendrite-free and flexible zinc-based energy storage, *Adv. Funct. Mater.* (2024) 2312855, <https://doi.org/10.1002/adfm.202312855>.
- [32] C. Yang, J. Yang, C. Liang, L. Zang, Z. Zhao, H. Li, L. Bai, Flexible supercapacitors with tunable capacitance based on reduced graphene oxide/tannin composite for wearable electronics, *J. Electroanal. Chem.* 894 (2021) 115354, <https://doi.org/10.1016/j.jelechem.2021.115354>.
- [33] X. Zhao, C. Huang, Q. Tang, Y. Hao, Y. Zhang, A. Hu, X. Chen, A simple approach towards highly dense graphene films for high volumetric performance supercapacitors, *ChemElectroChem* 9 (2022) e202101451.
- [34] J. Lemieux, D. Bélanger, C. Santato, Toward biosourced materials for electrochemical energy storage: The case of tannins, *ACS Sustainable Chem. Eng.* 9 (2021) 6079–6086, <https://doi.org/10.1021/acssuschemeng.1c01535>.
- [35] L. Wang, X. Chen, Three-dimensional activated graphite paper for high-performance supercapacitors, *J. Energy Storage* 52 (2022) 104939, <https://doi.org/10.1016/j.est.2022.104939>.
- [36] H. Zhang, Z. Wei, J. Wu, F. Cheng, Y. Ma, W. Liu, Y. Cheng, Y. Lin, N. Liu, Y. Gao, Y. Yue, Interlayer-spacing-regulated MXene/RGO foam for multi-functional zinc-ion microcapacitors, *Energy Storage Mater.* 50 (2022) 444–453, <https://doi.org/10.1016/j.ensm.2022.05.033>.
- [37] X. Zhong, Z. Kong, Q. Liu, C. Yang, Y. Chen, J. Qiu, L. Zang, Design strategy of high stability vertically aligned RGO@V₂O₅ heterostructure cathodes for flexible quasi-solid-state aqueous zinc-ion batteries, *ACS Appl. Mater. Interfaces* 15 (2023) 58333–58344, <https://doi.org/10.1021/acsami.3c12161>.
- [38] X. Sun, Y. Wan, B. Wang, Q. Xu, X. Teng, H. Liu, Y. Wang, S. Guo, C. Wu, H. Hu, M. Wu, Laser irradiation of graphite foils as robust current collectors for high-mass loaded electrodes of supercapacitors, *Rare Metals* 41 (2022) 4094, <https://doi.org/10.1007/s12598-022-02090-2>.
- [39] J. Hu, G. Kong, Y. Zhu, C. Che, Ultrafast room-temperature reduction of graphene oxide by sodium borohydride, sodium molybdate and hydrochloric acid, *Chin. Chem. Lett.* 32 (2021) 543–547, <https://doi.org/10.1016/j.cclet.2020.03.045>.
- [40] Z. Qiu, Z. Liu, G. Wang, C. Huangfu, Z. Li, Y. Yan, C. Chi, P. Gao, X. Lu, S. Zhang, T. Wei, Z. Fan, Highly redox-active oligomers between graphene sheets as ultrahigh capacitance/rate and stable electrodes for supercapacitors, *Energy Storage Mater.* 60 (2023) 102824, <https://doi.org/10.1016/j.ensm.2023.102824>.
- [41] R. Al-Gaashani, A. Najjar, Y. Zakaria, S. Mansour, M.A. Atieh, XPS and structural studies of high quality graphene oxide and reduced graphene oxide prepared by different chemical oxidation methods, *Ceram. Int.* 45 (2019) 14439–14448, <https://doi.org/10.1016/j.ceramint.2019.04.165>.
- [42] X. Zhang, C. Jiang, H. Li, X. Gan, W. Shi, Y. Liu, X. Yan, X. Zhao, B. Liu, Rational design of activated graphitic carbon spheres with optimized ion and electron transfer channels for zinc-ion hybrid capacitors, *J. Colloid Interface Sci.* 651 (2023) 211–220, <https://doi.org/10.1016/j.jcis.2023.07.140>.
- [43] X. Li, C. Cai, P. Hu, B. Zhang, P. Wu, H. Fan, Z. Chen, L. Zhou, L. Mai, H.J. Fan, Gradient pores enhance charge storage density of carbonaceous cathodes for Zinc-ion capacitor, *Adv. Mater.* (2024) 2400148, <https://doi.org/10.1002/adma.202400148>.
- [44] J. Wang, J. Polleux, J. Lim, B. Dunn, Pseudocapacitive contributions to electrochemical energy storage in TiO₂ (anatase) nanoparticles, *J. Phys. Chem. C* 111 (2007) 14925–14931, <https://doi.org/10.1021/jp074464w>.
- [45] X. Du, J. Shi, Z. Chen, T. Ni, J. Li, L. Ruan, W. Zeng, F. Cheng, Y. Yue, S. Wang, A laser etched zinc ion microbattery with excellent flexibility and self-healability, *Sustain. Energ. Fuels* 4 (2022) 4713–4721, <https://doi.org/10.1039/D0SE00843E>.
- [46] L. Le, Z. Cao, J. Li, H. Hu, D. Ho, Multiplying energy storage capacity: In situ polypyrrole electrodeposition for laser-induced graphene electrodes, *ACS Appl. Energ. Mater.* 5 (2022) 12790–12797, <https://doi.org/10.1021/acsam.2c02393>.
- [47] L. Li, W. Liu, K. Jiang, D. Chen, F. Qu, G. Shen, In-situ annealed Ti₃C₂T_x MXene based all-solid-state flexible Zn-ion hybrid micro supercapacitor array with enhanced stability, *Nano-Micro Lett.* 13 (2021) 100, <https://doi.org/10.1007/s40820-021-00634-2>.
- [48] P.B. Naik, P. Yadav, R. Nagaraj, R. Puttaswamy, H.K. Beere, U.N. Maiti, C. Mondal, N.S. Kotrappanavar, D. Ghosh, Developing high-performance flexible zinc ion capacitors from agricultural waste-derived carbon sheets, *ACS Sustain. Chem. Eng.* 10 (2022) 1471–1481, <https://doi.org/10.1021/acssuschemeng.1c06569>.
- [49] J. Shi, S. Wang, X. Chen, Z. Chen, X. Du, T. Ni, Q. Wang, L. Ruan, W. Zeng, Z. Huang, An ultrahigh energy density quasi-solid-state zinc ion microbattery with excellent flexibility and thermostability, *Adv. Energy Mater.* 9 (2019) 1901957, <https://doi.org/10.1002/aenm.201901957>.
- [50] Y. Zhou, W. Li, Y. Xie, L. Deng, B. Ke, Y. Jian, S. Cheng, B. Qu, X. Wang, Vertical graphene film enables high-performance quasi-solid-state planar zinc-ion microbatteries, *ACS Appl. Mater. Interfaces* 15 (2023) 9486–9493, <https://doi.org/10.1021/acsami.2c22043>.